FOUNDATIONS
ADVANCES

Volume 74 (2018)

Supporting information for article:

Structure evolution of h.c.p./c.c.p. metal oxide interfaces in solid-state reactions

C. Li, G. Habler, T. Griffiths, A. Rečnik, P. Jeřábek, L. C. Götze, C. Mangler, T. J. Pennycook, J. Meyer and R. Abart

Migration of *hcp*/*ccp* metal oxide interfaces via the glide of partial dislocations (Supplementary materials)

C. Li[a,b]*, G. Habler[a], T. Griffiths[a], A. Rečnik[c], P. Jeřábek[d], L. C. Götze[e], C. Mangler[f], T. J. Pennycook[f,b], J. Meyer[f], & R. Abart[a]

[a] Department of Lithospheric Research, University of Vienna, Althanstrasse 14, 1090 Vienna, Austria

[b] Stuttgart Center for Electron Microscopy, Max Planck Institute for Solid State Research, Heisenbergstr. 1, 70569 Stuttgart, Germany

[c] Department for Nanostructured Materials, Jožef Stefan Institute, Jamova cesta 39, SI-1000 Ljubljana, Slovenia

[d] Institute of Petrology and Structural Geology, Faculty of Science, Charles University, Albertov 6, 12843 Prague, Czech Republic

[e] Institute of Geological Sciences, Freie Universität Berlin, Malteserstr. 74-100,12249 Berlin, Germany

[f] Faculty of Physics, University of Vienna, Boltzmanngasse 5, 1090 Vienna, Austria

* Corresponding author. Email: chen.li@fkf.mpg.de

I. Details for material synthesis targeted at different growth stages

$MgAl_2O_4$ layers representing early and late growth stages were produced using two different methods.

In the first set of synthesis experiments, amorphous MgO was deposited using pulsed laser deposition (PLD) on polished (0001) single-crystal α-Al_2O_3 substrates. The method is described in detail by Götze in (Götze *et al.*, 2014), and only a brief summary is given here. Amorphous MgO was deposited on polished single-crystal α-Al_2O_3 substrates, with polished surfaces perpendicular to the [0001] c axis. Then the specimens were annealed at 800 to 1000°C for different durations. The heating and cooling rates were both 200K/min. No reaction occurred at 800°C. Reaction started at 900 °C, with $MgAl_2O_4$ layer thickness reaching 15-20 nm after 61 min. A series of $MgAl_2O_4$ layers from 20 to 400 nm depending on annealing time were grown at 1000 °C. In these experiments layer thickness increased at a constant rate, which we refer to as linear growth. Samples with linear growth representing the "interface-controlled" growth stages were selected for further microscopic investigations. These include the $MgAl_2O_4$ layers grown at 900°C for 61 minutes and at 1000°C for 5, 31, 120 and 180 minutes, the corresponding sample numbers of which are Cor26, Cor27, Cor29, Cor30 and Cor08 in (Götze *et al.*, 2014).

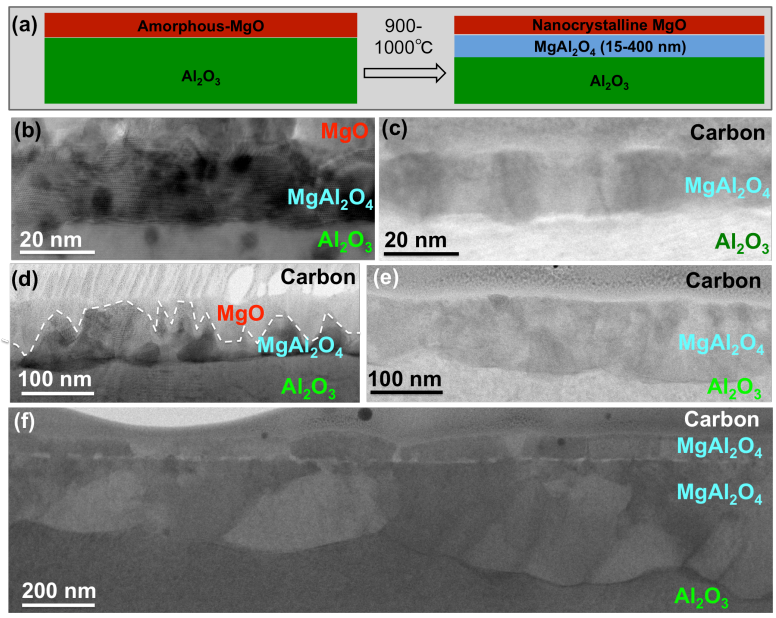

Supplemental Figure 1. Nanocrystalline $MgAl_2O_4$ layer on Al_2O_3 substrates grown by PLD. (a) A sketch showing the PLD growth method. STEM-bright field (BF) images show $MgAl_2O_4$ layers grown at (b) 900°C for 61 min; 1000°C for (c) 5, (d) 31, (e) 120 and (f) 180 min. The white dashed line in (d) indicates the position of the MgO/$MgAl_2O_4$ interface.

The $MgAl_2O_4$ thin-films produced using the PLD growth method represent the initial growth stages (Supplemental Figure 1 (a)). Supplemental Figure 1 (b-f) show the morphology of a series of PLD grown $MgAl_2O_4$ layers on Al_2O_3 substrates. At 900˚C, a $MgAl_2O_4$ layer about 15–20 nm thick was produced in one hour (Supplemental Figure 1(b)), with grain sizes of 5–20 nm. The $MgAl_2O_4$ layers grown at 1000˚C for 5, 31, 120, 180 min have thicknesses of 18–20nm, 20–100nm, 100–120nm, 200–400nm (Supplemental Figure 1(c-f)), with grain sizes of 10–20 nm, 20–100 nm, 40–100 nm and 50–400nm, respectively. Besides the grain size increase, the interface morphology also shows a change: with increasing annealing time the Al_2O_3/$MgAl_2O_4$ interfaces become successively more curved. The $MgAl_2O_4$ layers grown at 1000˚C for 180 min developed an internal structure line separating two domains within the layer. This layer-internal microstructure is similar to what is observed during the later growth stages as shown in section 3.2.1. Note that the amorphous MgO reactant layers in Supplemental Figure 1(c, e, f) have already been consumed. Very likely the PLD-deposited reactant layers of amorphous MgO have different thicknesses for different experimental runs. For the sample shown in Supplemental Figure 1(c), the amorphous MgO was presumably rather thin so that it was consumed after only a short reaction time. It is not clear why the interface between the $MgAl_2O_4$ layer and the MgO reactant layer is so curvy for the sample shown in Supplemental Figure 1(d), but the micron-scale

and nano-scale morphology at its $MgAl_2O_4/Al_2O_3$ interface is similar to other samples at the initial-growth stages.

The higher resolution images in Fig. 2 are from sample Cor26 that was heated at 900°C for 61 minutes. The higher resolution images in Figs. 3-5 are from sample Cor29 that was heated at 1000°C for 31 minutes.

In a second set of synthesis experiments, $MgAl_2O_4$ layers thicker than 10 µm were produced by the reaction of single-crystal MgO and single-crystal α-Al_2O_3 at 1350°C using a uniaxial load apparatus, which is referred to as conventional growth in the following part of the paper. The experimental procedure is described in detail in Jeřábek *et al.*, 2014, and briefly below. The [0001] axis of Al_2O_3 was aligned with one <100> axis of MgO, both axes were perpendicular to the contact surface and both contact surfaces were polished. The experiments were performed in a dry atmosphere maintained by a constant argon gas flow at 0.1 MPa pressure. The samples V27, V26 and CP28 from (Jeřábek *et al.*, 2014), which were annealed at 1350°C for 5, 20 and 80 hours respectively, were selected for the STEM study. The heating rate was 5 °C/min, and a constant load of 0.261kN was applied perpendicularly to the contact surfaces, which corresponds to a normal stress of 29 MPa for the 3 by 3 mm contact surface. After the growth of $MgAl_2O_4$, the samples were cut perpendicular to the crystal contact surfaces in order to prepare a chemo-mechanically polished thin section for electron backscatter diffraction (EBSD) analysis. The EBSD map in Fig. 6 is from sample CP28. Figs. 7 and 8 are from sample V27.

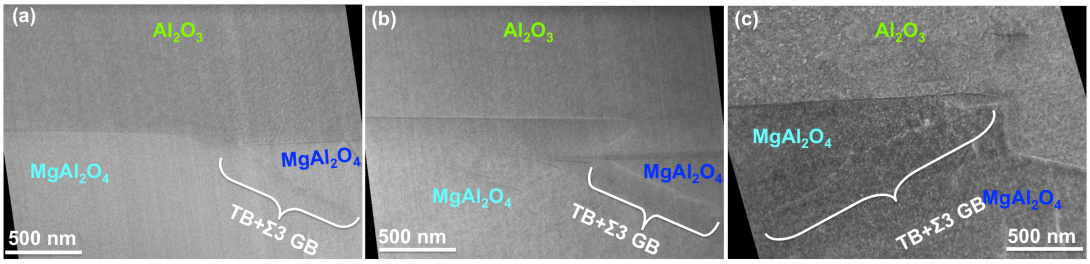

Supplemental Figure 2 (a-c) STEM-BF images show intersections of interface and "TB+ Σ3 GBs", where the interface facets change. (a-b) are from sample V27, (c) is from sample V26.

At the late growth stage, there is a typical feature at the $Al_2O_3/MgAl_2O_4$ interface: The $Al_2O_3/MgAl_2O_4$ interface typically changes its orientation at triple junctions, where it connects to a $MgAl_2O_4/MgAl_2O_4$ GB. Examples of such triple junctions are shown in low magnification in Supplemental Figure 2. The boundary between the two $MgAl_2O_4$ grains with twinning orientation relationship is formed by alternating segments of TBs (which are coherent Σ3 GBs with {111} facets at boundaries) and incoherent Σ3 GBs (referred to as Σ3 GBs in this work). The atomic

structures of the $Al_2O_3/MgAl_2O_4$ interface segments and of the $MgAl_2O_4/MgAl_2O_4$ GBs are shown in the atomic resolution Z-contrast images in Fig. 7 in the main article. Note that Fig. 7(d2) is composed of two images to show the long area at interface.

II. Details for electron microscopy and image process

Crystal orientation analysis was performed using FEI dual-beam Quanta 3D field emission gun (FEG) scanning electron microscope (SEM), at 15 kV accelerating voltage and about 2 nA probe current. The EBSD data were collected using the OIM data collection software v5.3.1. OIM, the analytical procedure and settings are described in (Jeřábek *et al.*, 2014). A focused ion beam (FIB) with OmniprobeTM 100.7 micromanipulator, also equipped on the FEI Quanta 3D FEG SEM, was used to extract specimens from the selected interface areas. Besides the common FIB lift-out with cross-section geometry, a plan-view lift-out geometry has also been applied to extract specimens (Li *et al.*, 2018) in order to study an interesting morphology of "$Al_2O_3/MgAl_2O_4/MgAl_2O_4$" triple junctions at the $Al_2O_3/MgAl_2O_4$ interface from late growth stage (Supplemental Figure 1). A 30 kV Ga-ion beam with high current (65 -1 nA) was used for the pre-cut, then 30 kV Ga-ion beam with lower current (1 nA- 50 pA) followed by 5 kV and 2 kV with low-current (48-27 pA) were used to thin the specimens to ~ 70nm. A low-kV (0.5-1 kV) argon-milling device was used for final thinning of the specimens to <50 nm thickness. A Nion UltraSTEM 5^{th}-order aberration-corrected STEM with sub-Å resolution (Krivanek *et al.*, 2011; 2008) was employed to resolve the atomic structure of the interface using accelerating voltage of 100 kV. Both bright field (BF) and high angle annular dark field (HAADF) detectors have been used for STEM imaging, the BF detector primarily for low-magnification imaging, and the HAADF detector primarily for atomic-resolution imaging. The probe-forming angle and the inner detector angle for the Z-contrast images were approximately 30 and 80 mrad respectively. Selected experimental images were processed for subsequent image analysis. Before image processing, STEM image distortions due to instrumental and environmental instabilities were corrected using the IMAGE-WARP procedure (Rečnik *et al.* 2005). Then, background intensity variations visible as horizontal stripes were extracted by filtering low frequency signal using DigitalMicrograph Software (Gatan Inc.) and Wiener Filter (Kilaas, 1998) to enhance signal-to-noise ratio of the experimental images.

III. Details for modeling and image simulations

The atomic models for image simulations were built by CrystalMaker. The crystallographic structure of α-Al_2O_3 and $MgAl_2O_4$ used in modeling are as below.

α-Al_2O_3, Space group R-3c

Unit cell parameters:
a: 4.7617 b: 4.7617 c: 12.9947 Å
alpha: 90.000 beta: 90.000 gamma: 120.000 degrees

			Fractional Coordinates			
Label	Site	Occupancy	x	y	z	Number In Cell
Al 1	Al	1.000	0.0000	0.0000	0.3521	12
O 1	O	1.000	0.3065	0.0000	0.2500	18

$MgAl_2O_4$, Space group F d -3 m

Unit cell parameters:
a: 8.08000; b: 8.08000; c: 8.08000 Å
alpha: 90.0000; beta: 90.0000; gamma: 90.0000 degrees

			Fractional Coordinates			
Label	Site	Occupancy	x	y	z	Number In Cell
Al 1	Al	1.000	0.50000	0.50000	0.50000	16
Mg 1	Mg	1.000	0.12500	0.12500	0.12500	8
O 1	O	1.000	0.26200	0.26200	0.26200	32

STEM HAADF image simulations were performed with Q-STEM software (Koch, 2002), using experimental settings for the according parameters.

When the oxygen sequence changes from an ABAB *hcp* lattice in Al_2O_3 to an ABCABC *ccp* lattice in $MgAl_2O_4$, there are six possible interface configurations. There are three possible oxygen sequences: A][BA][B(**A**]BC)(ABC), [AB][AB][(A**B**]C)(ABC), and A][BA][BA](CAB)(CAB), where [AB, or BA] and (ABC, or CAB) indicate stacking units in Al_2O_3 and $MgAl_2O_4$, respectively. For each oxygen sequence configuration, the terminating layer of $MgAl_2O_4$ at the interfaces can be either the pure Al layer or the Al+Mg mixed layer, describing as Al_2O_3-(Al-$MgAl_2O_4$) and Al_2O_3-(Mg-$MgAl_2O_4$) in Supplemental Figures 3 and 4. Therefore together there exist six types of interface configurations. The atomic models and corresponding simulated STEM HAADF images for all six are shown in Supplemental Figure 3.

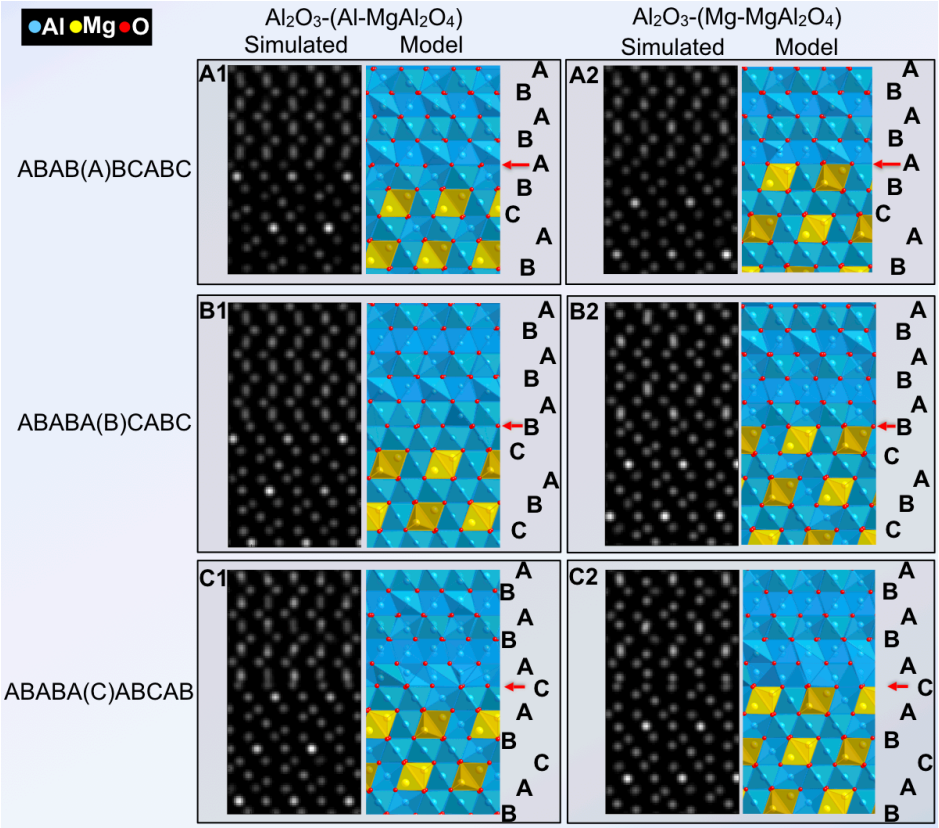

Supplemental Figure 3. Six possible interface structure: models and corresponding STEM-HAADF images.

We then compared the two types of experimentally observed interface structure in Fig. 3 (a1) and (b1) with the six possible interface configurations. The detailed comparison is shown in Supplemental Figure 4. We first compared the positions of the pure Al-layers and Al-Mg mixed layers in the direction perpendicular to the interfaces: for structure models A1, B2 and C2, only the experimental image in Fig. 3a1 matches; for structure models A2, B1 and C1, only the experimental image in Fig. 3b1 matches. Next we compared the positions of the atomic columns. The solid-green and dashed-yellow circles respectively indicate the extra and missing column positions in the simulated images in comparison to the experimental images. For the experimental image in Fig. 3b1, the atomic structure clearly matches simulated image of structure model B1. For another two possible models: there are extra Mg columns at interface plane in the simulated image of structure model A2, which are not observed in experimental image Fig. 3b1. Meanwhile there are columns missing in the simulated image of structure model A2. A similar thing is visible in the simulated image of structure model C1: clearly the columns at the interface plane do not match with those in experimental image Fig. 3b1. The interface structure in experimental image Fig. 3 (a1) is not as sharp as Fig. 3 (b1), which might be due to the 3D configuration of the

interface, for instance, the existence of interface steps along the beam direction. However the comparison of atomic structure away from the interface show which is the matching model. The positions of the fully occupied Al columns in the pure Al-layers of $MgAl_2O_4$ (brighter contrast in HAADF images) only match with the simulated image of structure model A1. For the simulated images of both structure models B2 and C2, there exists a shift of column positions in the horizontal direction (parallel with the interface plane). The models in Fig. 3(a) and (b) in the main text are same as the models A1 and B1 in Supplemental Figures 3 and 4.

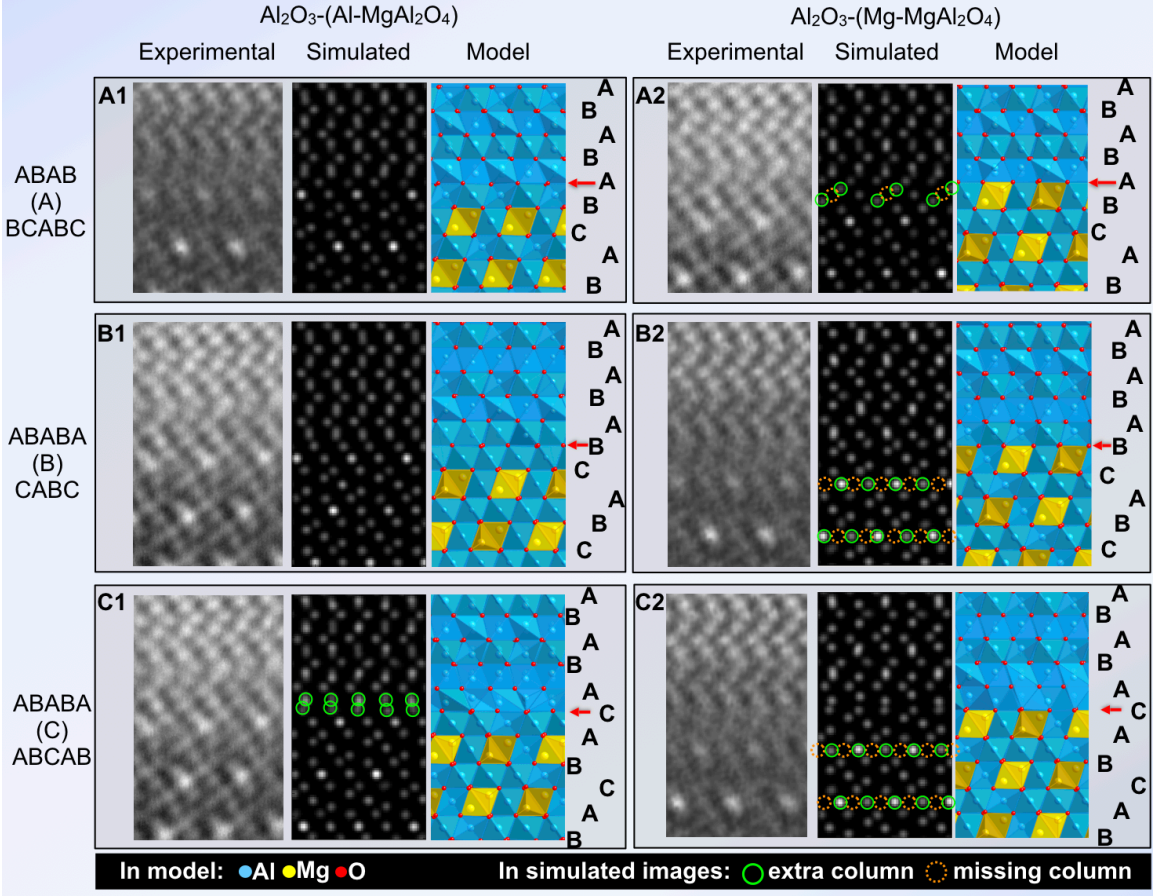

Supplemental Figure 4. Comparison between the two experimentally-observed interface structures and the simulated six possible structures in Supplemental Figure 3. The solid-green and dashed-yellow circles respectively indicate the extra and missing column positions in the simulated images in comparison to the experimental images.

IV. Fast Fourier Transformation (FFT) of HAADF images

To show the crystallographic relationship in reciprocal space, the corresponding FFT of $MgAl_2O_4$ and Al_2O_4 structures in different configurations are shown in below Supplemental Figure 5-8.

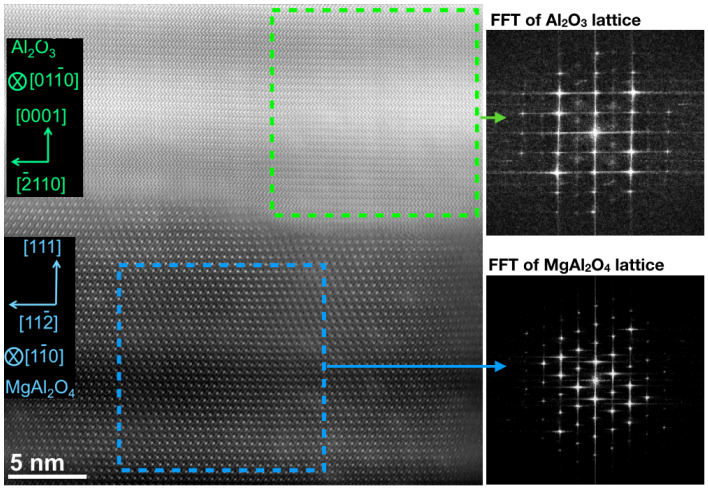

Supplemental Figure 5. FFT of $MgAl_2O_4$ and Al_2O_4 structures in Fig. 3 (d). The crystallographic relationships on Fig. 3(a-b) and Figs. 4 are same with that in Fig. 3 (d).

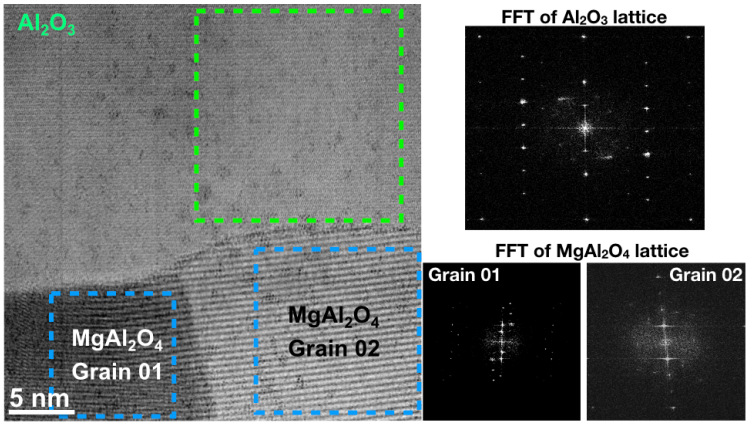

Supplemental Figure 6. FFT of $MgAl_2O_4$ and Al_2O_4 structures in Fig. 5 (a).

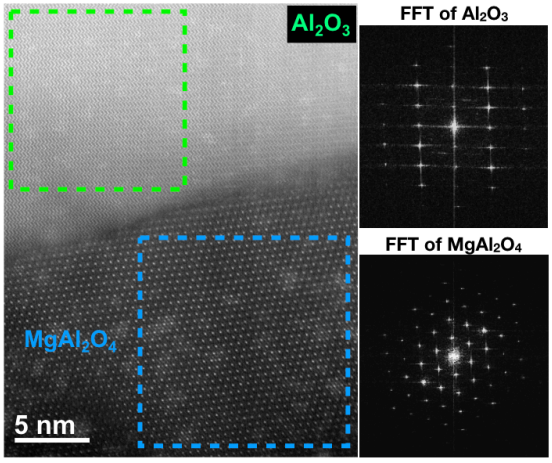

Supplemental Figure 7. FFT of $MgAl_2O_4$ and Al_2O_4 structures in Fig. 5 (b).

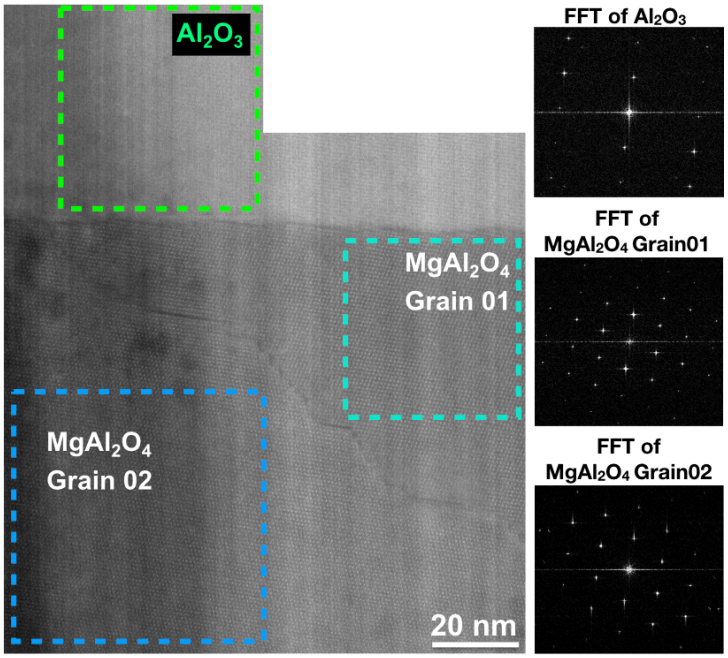

Supplemental Figure 8. FFT of $MgAl_2O_4$ and Al_2O_4 structures in Fig. 7.

References:

Götze, L. C., Abart, R., Milke, R., Schorr, S., Zizak, I., Dohmen, R. & Wirth, R. (2014). *Phys Chem Minerals*. **41**, 681–693.

Jeřábek, P., Abart, R., Rybacki, E. & Habler, G. (2014). *American Journal of Science*. **314**, 940–965.

Kilaas, R. (1998). *Journal of Microscopy*. **190**, 45–51.

Koch, C. (2002). Determination of Core Structure Periodicity and Point Defect Density Along Dislocations. Arizona State University.

Krivanek, O. L., Chisholm, M. F., Dellby, N. & Murfitt, M. F. (2011). Scanning transmission electron microscopy Imaging and Analysis New York, NY: Springer.

Krivanek, O. L., Corbin, G. J., Dellby, N., Elston, B. F., Keyse, R. J., Murfitt, M. F., Own, C. S., Szilagyi, Z. S. & Woodruff, J. W. (2008). *Ultramicroscopy*. **108**, 179–195.

Li, C., Habler, G., Baldwin, L. C. & Abart, R. (2018). *Ultramicroscopy*. **184**, 310–317.